Revisiting the Kitaev material candidacy of Ir^{4+} double perovskite iridates

A. A. Aczel,[1,2,*] J. P. Clancy,[3,†] Q. Chen,[2] H. D. Zhou,[2] D. Reig-i-Plessis,[4] G. J. MacDougall,[4] J. P. C. Ruff,[5]
M. H. Upton,[6] Z. Islam,[6] T. J. Williams,[1] S. Calder,[1] and J.-Q. Yan[7]

[1]*Neutron Scattering Division, Oak Ridge National Laboratory, Oak Ridge, Tennessee 37831, USA*
[2]*Department of Physics and Astronomy, University of Tennessee, Knoxville, Tennessee 37996, USA*
[3]*Department of Physics and Astronomy, McMaster University, Hamilton, Ontario, Canada L8S 4M1*
[4]*Department of Physics, University of Illinois at Urbana-Champaign, Urbana, Illinois 61801, USA*
[5]*Cornell High Energy Synchrotron Source, Cornell University, Ithaca, New York 14853, USA*
[6]*Advanced Photon Source, Argonne National Laboratory, Lemont, Illinois 60439, USA*
[7]*Materials Science and Technology Division, Oak Ridge National Laboratory, Oak Ridge, Tennessee 37831, USA*

Quantum magnets with significant bond-directional Ising interactions, so-called Kitaev materials, have attracted tremendous attention recently in the search for exotic spin liquid states. Here we present a comprehensive set of measurements that enables us to investigate the crystal structures, Ir^{4+} single-ion properties, and magnetic ground states of the double perovskite iridates La_2BIrO_6 ($B =$ Mg, Zn) and A_2CeIrO_6 ($A =$ Ba, Sr) with a large nearest-neighbor distance >5 Å between Ir^{4+} ions. Our neutron powder diffraction data on Ba_2CeIrO_6 can be refined in the cubic space group $Fm\bar{3}m$, while the other three systems are characterized by weak monoclinic structural distortions. Despite the variance in the noncubic crystal field experienced by the Ir^{4+} ions in these materials, x-ray absorption spectroscopy and resonant inelastic x-ray scattering are consistent with $J_{\mathrm{eff}} = 1/2$ moments in all cases. Furthermore, neutron scattering and resonant magnetic x-ray scattering show that these systems host A-type antiferromagnetic order. These electronic and magnetic ground states are consistent with expectations for face-centered-cubic magnets with significant antiferromagnetic Kitaev exchange, which indicates that spacing magnetic ions far apart may be a promising design principle for uncovering additional Kitaev materials.

I. INTRODUCTION

Kitaev materials are quantum magnets with significant nearest-neighbor (NN), bond-directional Ising interactions [1,2]. The Kitaev Hamiltonian may be a useful starting point for describing the often exotic magnetic properties of these materials. Notably, for the special cases of the quasi-two-dimensional (quasi-2D) honeycomb lattice [3] or its three-dimensional (3D) honeycomb variants [4,5], these models are exactly soluble and yield a Kitaev spin-liquid ground state for either antiferromagnetic (AFM) or ferromagnetic (FM) Kitaev couplings. Numerical approaches or theoretical approximations have been employed to investigate the Kitaev model in other symmetry-allowed cases, revealing a chiral spin liquid [6] or nematic phase [7–9] for an AFM Kitaev interaction on the triangular lattice, and an unidentified quantum phase with an extensive degeneracy on the hyperkagome lattice for either AFM or FM Kitaev exchange [10]. The AFM Kitaev models on the kagome and pyrochlore lattices are geometrically frustrated and their ground states are still unknown [10].

Pioneering work by Jackeli and Khaliullin [11] provided crucial insights on how to search for new Kitaev materials. Strong electronic correlations and spin-orbit coupling (SOC)

can produce $J_{\mathrm{eff}} = 1/2$ spin-orbit-assisted Mott insulating states [12] in heavy transition-metal (TM) magnets based on Ir^{4+} or Ru^{3+} in an ideal octahedral local environment. The combination of $J_{\mathrm{eff}} = 1/2$ single-ion wave functions and edge-sharing TM-ligand octahedra leads to a complete cancellation of the conventional Heisenberg superexchange via TM-ligand-TM pathways, thus ensuring that the effective magnetic interaction is highly anisotropic and depends on the spatial orientation of a given bond.

The quasi-2D honeycomb systems Na_2IrO_3 [13,14], α-Li_2IrO_3 [15,16], and α-$RuCl_3$ [17–20], as well as the 3D honeycomb variants β-Li_2IrO_3 [21,22] and γ-Li_2IrO_3 [23,24], have been characterized as potential Kitaev materials. This breakthrough started an ongoing quest to search for a Kitaev spin liquid in the laboratory, with the hope of identifying and characterizing the elusive Majorana fermion quasiparticles associated with this state for possible applications in quantum computing. Although it is now well-known that these materials host ordered magnetic ground states due to additional competing interactions, including NN symmetric off-diagonal exchange Γ, NN Heisenberg direct exchange, and further-neighbor Heisenberg exchange, there have been some promising developments more recently. Inelastic neutron scattering [20,25] and Raman spectroscopy measurements [26] have shown that α-$RuCl_3$ is proximate to the desired Kitaev spin-liquid state, as a broad continuum of magnetic scattering has been identified and attributed to fractionalized Majorana
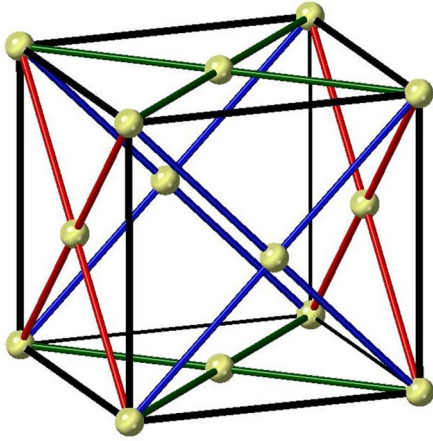
FIG. 1. A schematic of the ideal fcc crystal structure showing how NN Kitaev exchange can arise in this case. The colored bonds correspond to bond-directional Ising interactions between the different spin components S_x, S_y, or S_z. For simplicity, the bonds going through the cube are not shown.

fermion excitations. Complementary studies on α-RuCl$_3$ have shown that external perturbations, including a magnetic field [27], chemical doping [28], and pressure [29], can suppress the zigzag magnetic order and therefore provide a viable way to tune the magnetic Hamiltonian. Additional quasi-2D honeycomb iridates have also been discovered, including Cu$_2$IrO$_3$ [30] and H$_3$LiIr$_2$O$_6$ [31], and the initial characterization work has identified dynamical quantum disordered ground states [31–33]. While these results are not inconsistent with Kitaev spin-liquid physics, significant structural disorder may complicate the picture in both compounds and therefore needs to be better understood.

Recent work on the ideal 6H-perovskite structure, originally thought to be relevant to Ba$_3$IrTi$_2$O$_9$ [8], has shown that materials with adjacent TM-ligand octahedra with parallel edges may also be capable of hosting significant Kitaev interactions. This local geometry for the Ir^{4+} ions ensures that they are coupled through two extended superexchange paths of the form TM-ligand-ligand-TM, possibly leading to a significantly reduced value for the NN Heisenberg superexchange. It is also tantalizing that spacing the magnetic atoms further apart may lead to the suppression of direct exchange contributions from NN Heisenberg and off-diagonal Γ terms, possibly leading to the discovery of Kitaev materials in other structures beyond the honeycomb lattice. While significant Ir/Ti site disorder ensures that Ba$_3$IrTi$_2$O$_9$ [34,35] does not crystallize in the ideal 6H-perovskite structure required for the triangular lattice Kitaev model, the ideas presented in Ref. [8] led to detailed studies of the double perovskite iridates La$_2$MgIrO$_6$ and La$_2$ZnIrO$_6$ in the context of the face-centered-cubic (fcc) Kitaev model [36–38]. Adjacent IrO$_6$ octahedra share parallel edges in the ideal fcc structure, and therefore significant NN Kitaev exchange is possible according to the schematic presented in Fig. 1. Despite small monoclinic structural distortions leading to noncubic crystal fields at the Ir^{4+} sites [36,39], the classical phase diagram for the fcc Heisenberg-Kitaev-Γ model with $J_{\text{eff}} = 1/2$ moments is

consistent with the *A*-type AFM ordered states [37] observed in these compounds. Similarly, a magnetic Hamiltonian with a dominant NN AFM Kitaev interaction can explain the Weiss temperatures, the AFM ordering temperatures ($T_N = 12$ and 7.5 K for the Mg and Zn systems, respectively [36]), and the dynamical structure factors measured with inelastic neutron scattering [38].

Ba$_2$CeIrO$_6$ and Sr$_2$CeIrO$_6$ are two other double perovskites with an Ir^{4+} valence inferred from x-ray diffraction measurements [40,41], and therefore they are also promising candidates for fcc Kitaev materials based on extended superexchange interactions. Both systems were found to exhibit long-range AFM order, with $T_N = 17$ and 21 K for the Ba [40] and Sr [41] analogs, respectively, although the magnetic structures have yet to be determined. Surprisingly, Ba$_2$CeIrO$_6$ has not been discussed in the context of $J_{\text{eff}} = 1/2$ magnetism. On the other hand, two different DFT studies have investigated the $J_{\text{eff}} = 1/2$ scenario for Sr$_2$CeIrO$_6$ [42,43]. While both studies find that electronic correlations and SOC are key ingredients for establishing an AFM insulator, Ref. [42] supports $J_{\text{eff}} = 1/2$ magnetism while Ref. [43] argues that significant *c*-axis compression of the IrO$_6$ octahedra in Sr$_2$CeIrO$_6$ leads to a breakdown of this state and promotes "weak" orbital ordering instead.

Due to the nearly cubic crystal field environment for Ir^{4+} in the four double perovskite iridates described above, it would be surprising to find significant deviations from $J_{\text{eff}} = 1/2$ magnetism in any of these materials, but there are inconsistencies in the published crystal structures (e.g., Ba$_2$CeIrO$_6$ has been reported to crystallize in both cubic [44] and monoclinic [40] space groups), and direct experimental proof of the Ir^{4+} $J_{\text{eff}} = 1/2$ electronic ground states is lacking. Also, there is only limited information available on the collective magnetic properties of these interesting fcc Kitaev material candidates. Therefore, we have revisited their low-temperature crystal structures with neutron powder diffraction (NPD) and assessed their $J_{\text{eff}} = 1/2$ candidacy using a combination of x-ray absorption spectroscopy (XAS) and resonant inelastic x-ray scattering (RIXS). We also used scattering techniques to determine the magnetic structures of La$_2$MgIrO$_6$, Ba$_2$CeIrO$_6$, and Sr$_2$CeIrO$_6$. Finally, we performed an inelastic neutron scattering experiment on polycrystalline samples of Ba$_2$CeIrO$_6$ and Sr$_2$CeIrO$_6$, using the same experimental configuration previously reported for La$_2$MgIrO$_6$ and La$_2$ZnIrO$_6$ [38], in an effort to gain insight into the evolution of the spin waves and hence the magnetic Hamiltonians of the Ce samples relative to the La analogs.

II. EXPERIMENTAL DETAILS

Polycrystalline samples of La$_2$MgIrO$_6$, La$_2$ZnIrO$_6$, Ba$_2$CeIrO$_6$, and Sr$_2$CeIrO$_6$ were synthesized by conventional solid-state reactions. The detailed procedure for synthesizing La$_2$MgIrO$_6$ and La$_2$ZnIrO$_6$ is presented in Ref. [36]. For Ba$_2$CeIrO$_6$ and Sr$_2$CeIrO$_6$, the starting materials ACO$_3$ (A = Ba, Sr), CeO$_2$, and IrO$_2$ were first mixed in the appropriate molar ratio. The homogeneous powder was then pelletized, placed in a covered alumina crucible, and heated to 1200 °C in 20 h and held at this temperature for 60 h. The heating process was repeated again after

one intermediate grinding. X-ray powder diffraction measurements verified that all four polycrystalline samples were single-phase, and magnetic susceptibility measurements using a Quantum Design magnetic property measurement system (MPMS) confirmed the AFM ordering temperatures reported previously [36,40,41].

Single crystals of La_2MgIrO_6 were grown by a flux method using a stoichiometric amount of the starting materials La_2O_3, MgO, and Ir with purities not less than 99.9%. A mixture of $PbO-PbF_2$ with a molar ratio of 1:1 was used as the flux by combining it with the starting materials in a 6:1 mass ratio. The mixed powder was placed into a covered platinum crucible and heated to 1220 at 120 °C/h, left at the target temperature for 24 h, and then cooled down to 500 at 15 °C/h. The furnace was then turned off and the crystals were separated from the flux with a centrifuge. They typically had an octahedral geometry, and all dimensions were less than 1 mm. X-ray powder diffraction measurements on crushed single crystals verified phase purity, and magnetic susceptibility measurements using a Quantum Design MPMS confirmed that the ordering temperature was consistent with both previous and current results on polycrystalline samples. Unfortunately, attempts to grow single crystals of the other three compositions using a similar flux procedure were unsuccessful.

Neutron powder diffraction (NPD) was performed with ~5 g of polycrystalline La_2MgIrO_6, La_2ZnIrO_6, and Ba_2CeIrO_6 and ~2.5 g of polycrystalline Sr_2CeIrO_6 using the HB-2A powder diffractometer of the High Flux Isotope Reactor (HFIR) at Oak Ridge National Laboratory (ORNL) to revisit the crystal structures of these materials systematically. The samples were loaded in cylindrical vanadium cans with 5 mm inner diameters. The data were collected at $T = 4$ K with a neutron wavelength of 1.54 Å and slightly different collimations of 12′-21′-6′ for La_2MgIrO_6 and La_2ZnIrO_6 and open-21′-12′ for Ba_2CeIrO_6 and Sr_2CeIrO_6.

X-ray absorption spectroscopy (XAS) was performed on polycrystalline samples of La_2MgIrO_6, La_2ZnIrO_6, Ba_2CeIrO_6, and Sr_2CeIrO_6 at room temperature using the A2 beamline at the Cornell High Energy Synchrotron Source (CHESS) to assess the importance of spin-orbit coupling to their Ir^{4+} electronic ground states. Measurements were collected at both the L_2 ($2p_{1/2} \rightarrow 5d$) and L_3 ($2p_{3/2} \rightarrow 5d$) Ir absorption edges, which occur at energies of 12.824 and 11.215 keV, respectively. The energy of the incident x-ray beam was selected using a diamond-(1 1 1) double crystal monochromator, with higher harmonic contributions suppressed by a combination of Rh-coated mirrors and a 50% detuning of the second monochromator crystal. The XAS measurements were performed in transmission geometry, using a series of three ion chambers (I_0, I_1, and I_2). The sample was mounted between I_0 and I_1, while an elemental Ir reference sample was mounted between I_1 and I_2. This configuration allows a direct measurement of the linear x-ray attenuation coefficient, $\mu(E)$, which is defined by the intensity ratio of the incident and transmitted x-ray beams. In this case, $\mu_{sample}(E) = I_0/I_1$ and $\mu_{Ir}(E) = I_1/I_2$. The energy calibration of this setup is accurate to within 0.25 eV, and direct comparisons between sample and reference spectra can be used to rule out any systematic energy drifts over the course of the experiment.

Resonant inelastic x-ray scattering (RIXS) measurements were conducted on polycrystalline samples of La_2MgIrO_6, La_2ZnIrO_6, Ba_2CeIrO_6, and Sr_2CeIrO_6 at room temperature using the MERIX spectrometer on beamline 27-ID of the Advanced Photon Source (APS) at Argonne National Laboratory to investigate the Ir^{4+} crystal-field excitations. The incident x-ray energy was tuned to the Ir L_3 absorption edge at 11.215 keV. A double-bounce diamond-(1 1 1) primary monochromator, a channel-cut Si-(8 4 4) secondary monochromator, and a spherical (2 m radius) diced Si-(8 4 4) analyzer crystal were used to obtain an overall energy resolution of ~35 meV [full width at half-maximum (FWHM)]. To minimize the elastic background intensity, measurements were carried out in horizontal scattering geometry with the scattering angle 2θ set to 90°.

Resonant magnetic x-ray scattering (RMXS) measurements were performed on a single crystal of La_2MgIrO_6 using beamline 6-ID-B at the APS to determine the magnetic structure of this material. The incident x-ray energy was tuned to the Ir L_3 absorption edge at 11.215 keV. Measurements were carried out in vertical scattering geometry, using incident photons that were linearly polarized perpendicular to the scattering plane (i.e., σ polarization). In this geometry, resonant magnetic scattering rotates the plane of linear polarization into the scattering plane (i.e., π polarization). In contrast, charge scattering does not change the polarization of the scattered photons. As a result, polarization analysis of the scattered beam can be used to distinguish the magnetic (σ-π) and charge (σ-σ) scattering contributions. The (0 0 8) reflection from pyrolytic graphite (PG) was used as a polarization and energy analyzer. The sample was mounted on the cold finger of a closed-cycle refrigerator capable of reaching temperatures from 6 to 300 K. We were able to identify a crystal with a surface normal corresponding to the [1 1 0] direction (indexed in $P2_1/n$ monoclinic notation) for this experiment. Our measurements primarily focused on reflections close to this surface normal direction.

Elastic neutron scattering measurements, complementary to the NPD experiment described above, were performed on the 14.6 meV fixed-incident-energy triple-axis spectrometer HB-1A of the HFIR at ORNL using the same polycrystalline samples of Ba_2CeIrO_6 and Sr_2CeIrO_6 studied at HB-2A. Since the main goal of this experiment was to determine the magnetic structures of these materials, these samples were loaded in Al cans with a 1-mm-thick annulus to minimize neutron absorption. The background was also minimized by using a double-bounce monochromator system, mounting two highly oriented PG filters in the incident beam to remove higher-order wavelength contamination, and placing a PG analyzer crystal before the single He-3 detector for energy discrimination. A collimation of 40′-40′-80′-open resulted in an energy resolution at the elastic line just over 1 meV (FWHM). The elastic scattering was measured at 4 and 30 K for both samples.

Inelastic neutron scattering (INS) spectra were measured with the HYSPEC spectrometer at the Spallation Neutron Source of ORNL using ~5 g of polycrystalline Ba_2CeIrO_6 and Sr_2CeIrO_6 loaded into the annular cans described above. All data were collected using incident energies of $E_i = 7.5$ and 15 meV, with corresponding Fermi chopper frequencies of

240 and 300 Hz, resulting in instrumental energy resolutions of 0.3 and 0.7 meV (FWHM), respectively, at the elastic line. A He cryostat was used to achieve a base temperature of 1.5 K. Empty Al annular can measurements were subtracted from all the HYSPEC data presented in this work to minimize the Al scattering contribution to the sample spectra.

III. CRYSTAL STRUCTURES

B/B'-site ordered double perovskites, with the general formula $A_2BB'O_6$, may crystallize in an ideal fcc structure or lower-symmetry variants. Detailed knowledge of the Ir^{4+} local environment is crucial for properly assessing the $J_{eff} = 1/2$ candidacy of the double perovskite iridates La_2MgIrO_6, La_2ZnIrO_6, Ba_2CeIrO_6, and Sr_2CeIrO_6, as significant noncubic crystal fields at the Ir^{4+} sites can lead to deviations in the electronic wave functions expected for this desired single-ion ground state. It is also important to characterize symmetry-lowering structural distortions away from an ideal fcc lattice since they can lead to additional NN interactions between Ir ions beyond those captured in the Heisenberg-Kitaev-Γ model (e.g., anisotropic Kitaev exchange [38]). The crystal structures have been determined previously by room-temperature x-ray powder diffraction [36,40,41,44,45] and variable temperature neutron powder diffraction [39,43,46]. Most refinements show that these materials exhibit very small monoclinic distortions away from the ideal fcc structure, although Ba_2CeIrO_6 has been reported to crystallize in both cubic [44] and monoclinic [40] space groups. Some variation has also been found in the structural parameters crucial for establishing $J_{eff} = 1/2$ electronic ground states in these materials, such as the oxygen fractional coordinates, Ir-O bond lengths, and O-Ir-O bond angles. X-ray diffraction is not the optimal technique for determining these parameters due to the weak x-ray scattering power of oxygen, while the specific sample geometry used in a NPD experiment affects the relative intensities of the Bragg peaks due to the significant neutron absorption expected from iridium, and this introduces systematic error into the refinements. Some previous diffraction work has also assumed no B/B'-site mixing [39,46], even though it is a common feature of this crystal structure. Therefore, an NPD study where the crystal structures of these materials are revisited with a consistent sample geometry is highly warranted, so the results can be compared on an equal footing.

Figure 2 shows HB-2A NPD data as solid red squares collected using a neutron wavelength of 1.54 Å for all four double perovskite iridates with $T = 4$ K. A common sample geometry was used for these measurements with each composition loaded in a cylindrical vanadium can with a 5 mm inner diameter. Rietveld refinement results performed using FULLPROF [47] are superimposed on the data as black solid curves. Table I shows lattice constants, atomic fractional coordinates, and selected bond distances and angles extracted from the refinements. We find that the Ba_2CeIrO_6 data refine well in the space group $Fm\bar{3}m$ corresponding to the ideal fcc structure, which implies that the Ir^{4+} ions in this material have cubic point symmetry and hence a $J_{eff} = 1/2$ electronic ground state. In sharp contrast, the diffraction data for the other three materials are better described by the monoclinic $P2_1/n$ space group. Significant B/B' site mixing is found
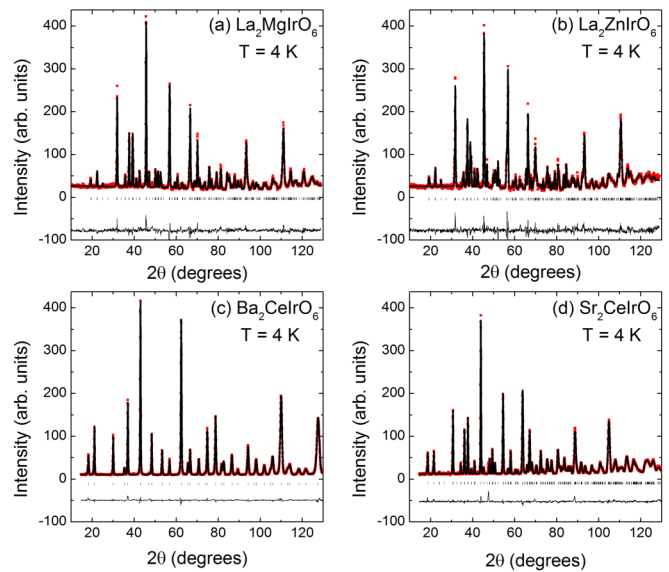

FIG. 2. Neutron powder diffraction data, indicated by the solid symbols and collected with a neutron wavelength 1.54 Å at a temperature $T = 4$ K, are shown for (a) La_2MgIrO_6, (b) La_2ZnIrO_6, (c) Ba_2CeIrO_6, and (d) Sr_2CeIrO_6. The best structural refinements are superimposed on the data as solid curves, the difference curves are shown below the diffraction patterns, and the expected Bragg peak positions are indicated by ticks.

in La_2MgIrO_6 (20%) and La_2ZnIrO_6 (14%), which is larger than past estimates from x-ray diffraction [38] but agrees well with NPD results on the related materials Sr_2MgIrO_6 and Sr_2ZnIrO_6 [48]. No B/B'-site mixing is found in Ba_2CeIrO_6 or Sr_2CeIrO_6. The amount of B/B' site mixing inversely tracks the B/B' ionic radii (r) differences in these materials, as $r_{Ce^{4+}} > r_{Zn^{2+}} > r_{Mg^{2+}} > r_{Ir^{4+}}$ [49]. No extra Bragg peaks indicative of magnetic order are observed in these data, likely due to extremely small ordered moments.

Typically, structural distortions arise in B/B'-site ordered double perovskites due to a small A-site cation, with the ideal $Fm\bar{3}m$ fcc structure often becoming tetragonal $I4/m$ or monoclinic $P2_1/n$. Table I shows that the double perovskite iridates studied here follow this general trend, as the structural distortions become larger when the ionic radius of the A site decreases (i.e., $r_{Ba^{2+}} > r_{Sr^{2+}} > r_{La^{3+}}$) [49]. Assuming that $\hat{x}, \hat{y}$, and $\hat{z}$ are aligned with the three fcc crystallographic directions, the relationships between the tetragonal and fcc lattice vectors are as follows: $\boldsymbol{a}_t = a_{fcc}(\hat{x} \pm \hat{y})/2$ and $\boldsymbol{c}_t = a_{fcc}\hat{z}$. The monoclinic structure is then derived from the tetragonal unit cell by simply modifying the lattice constants such that $\boldsymbol{a} \neq \boldsymbol{b}$ and $\beta \neq 90°$. The $B'O_6$ octahedra are both distorted and rotated as a consequence of the symmetry-lowering.

The noncubic crystal fields Δ at the Ir^{4+} sites in the monoclinic double perovskite iridates, which may lead to possible deviations from $J_{eff} = 1/2$ magnetism, arise from IrO_6 octahedral distortions only. The relative magnitudes and signs of Δ can be determined by comparing Ir-O bond lengths and O-Ir-O bond angles associated with these octahedra. Our refinement results reported in Table I show that all six Ir-O bond lengths for the three monoclinic double perovskite iridates are within 2% of each other, while all O-Ir-O bond

TABLE I. Structural parameters for La_2BIrO_6 ($B = Mg, Zn$) and A_2CeIrO_6 ($A = Ba, Sr$) extracted from the refinements of the 1.54 Å neutron powder diffraction data. The lattice constants and bond distances are in Å and all angles are in degrees.

Material	La-Mg	La-Zn	Ba-Ce	Sr-Ce
Space group	$P2_1/n$	$P2_1/n$	$Fm\bar{3}m$	$P2_1/n$
a	5.5874(2)	5.5917(2)	8.4126(1)	5.8243(2)
b	5.6307(2)	5.6912(2)	8.4126(1)	5.8400(2)
c	7.9119(3)	7.9335(3)	8.4126(1)	8.2395(3)
β	90.01(1)	90.03(1)	90	90.266(3)
$A\ x$	0.512(1)	0.5112(9)	0.25	0.5074(8)
$A\ y$	0.5411(5)	0.5497(5)	0.25	0.5336(4)
$A\ z$	0.253(2)	0.248(1)	0.25	0.2460(8)
B	(0.5,0,0)	(0.5,0,0)	(0.5,0.5,0.5)	(0.5,0,0.5)
Ir	(0.5,0,0.5)	(0.5,0,0.5)	(0,0,0)	(0.5,0,0)
$O_1\ x$	0.215(2)	0.200(2)	0.2390(1)	0.226(1)
$O_1\ y$	0.221(2)	0.214(2)	0	0.2053(9)
$O_1\ z$	0.951(1)	0.945(1)	0	0.9636(7)
$O_2\ x$	0.295(2)	0.293(2)	0.2390(1)	0.3005(9)
$O_2\ y$	0.699(2)	0.699(2)	0	0.726(1)
$O_2\ z$	0.964(1)	0.963(1)	0	0.9598(6)
$O_3\ x$	0.420(1)	0.410(1)	0.2390(1)	0.4259(9)
$O_3\ y$	0.986(1)	0.980(1)	0	0.9847(7)
$O_3\ z$	0.256(2)	0.254(2)	0	0.2368(6)
Site mixing	20(3)%	14(3)%	0	0
R_{wp}	8.15%	9.65%	4.40%	6.38%
χ^2	1.67	2.28	6.32	9.20
$Ir\text{-}O_1$	2.02(1)	2.02(1)	2.010(1)	2.018(6)
$Ir\text{-}O_2$	2.01(1)	2.01(1)	2.010(1)	2.007(6)
$Ir\text{-}O_3$	1.98(2)	2.02(2)	2.010(1)	2.002(5)
$O_1\text{-}Ir\text{-}O_2$	94.7(8)	91.6(8)	90	90.4(4)
$O_2\text{-}Ir\text{-}O_3$	91.3(8)	91.7(8)	90	90.1(4)
$O_1\text{-}Ir\text{-}O_3$	91.3(9)	91.5(9)	90	90.2(4)
$w(Ir)$	9	11		9
$j(Ir)$	13	14		12

angles are within 4.7° (La_2MgIrO_6), 1.7° (La_2ZnIrO_6), or 0.4° (Sr_2CeIrO_6) of the ideal 90° and 180° values. These deviations from an Ir^{4+} cubic crystal-field environment are smaller than or comparable to the IrO_6 octahedral distortions measured in the $J_{eff} = 1/2$ magnets Na_2IrO_3 [50] and Sr_2IrO_4 [51], and therefore these diffraction results provide indirect evidence that the $J_{eff} = 1/2$ description applies to the monoclinic double perovskite iridates described here.

The monoclinic structure also ensures that adjacent IrO_6 octahedra no longer have parallel edges, which can have a significant effect on the exchange interactions. Both the IrO_6 octahedral distortions and rotations described above can play a role here. The IrO_6 octahedral distortions have already been quantified in La_2MgIrO_6, La_2ZnIrO_6, and Sr_2CeIrO_6 as explained above, while the octahedral rotations can be determined according to Ref. [52] by using the refined atomic fractional coordinates and the Glazer notation discussed in Refs. [53,54]. We find that the IrO_6 octahedra are subjected to a global rotation $j(Ir)$ about the b axis and another rotation $w(Ir)$ about the c axis that is staggered between adjacent ab layers; the magnitude of these rotations is shown in Table I. Overall, our results indicate that the monoclinic

double perovskite iridates are characterized by very weak IrO_6 octahedral distortions but significant IrO_6 octahedral rotations, and therefore the latter effect will lead to the largest deviations in the collective magnetic properties expected for ideal fcc systems.

IV. SINGLE-ION PROPERTIES

Despite the perceived importance of spin-orbit coupling effects in La_2MgIrO_6, La_2ZnIrO_6, Ba_2CeIrO_6, and Sr_2CeIrO_6, no attempt has been made to measure the strength of the spin-orbit interactions in these compounds. One established technique for accomplishing this task is x-ray absorption spectroscopy (XAS), as it was shown that the integrated intensity ratio of the white line features measured at the L_2 and L_3 absorption edges (i.e., the branching ratio BR $= I_{L_3}/I_{L_2}$) is directly proportional to the expectation value of the spin-orbit coupling operator $\langle \boldsymbol{L} \cdot \boldsymbol{S} \rangle$ [55–57]. More specifically, the branching ratio can be written as BR $= (2 + r)/(1 - r)$, where $r = \langle \boldsymbol{L} \cdot \boldsymbol{S} \rangle / \langle n_h \rangle$, and n_h is the number of holes in the valence shell. A branching ratio significantly greater than 2 indicates a strong coupling between the local orbital and spin moments in the electronic ground state of the transition metal under investigation. However, the converse is not necessarily true (i.e., a statistical BR can arise even in the presence of strong spin-orbit coupling if the electronic bandwidth is sufficiently large or the spin or orbital moments are quenched).

Figure 3 shows the x-ray absorption spectra at the Ir L_3 and L_2 edges, plotted as the linear x-ray attenuation coefficient $\mu(E)$ versus energy, for all four double perovskite iridates. The data were normalized to absorption steps of 1 for both the L_3 and L_2 edges. To extract the BR from our data, we followed the procedure described in Ref. [58]. More specifically, we fit the near-edge portion of each spectrum to the following expression:

$$\mu(E) = C_0 + C_1 E + C_2 \arctan\left(\frac{E - E_0}{\Gamma/2}\right) + \frac{C_3}{1 + \left(\frac{E - E_0}{\Gamma/2}\right)^2},$$

(1)

where C_0 and C_1 represent a linear background, C_2 is the absorption step height, C_3 is the white-line intensity, and E_0 and Γ correspond to the center and width of both the arctangent and Lorentzian functions. A secondary measure of the
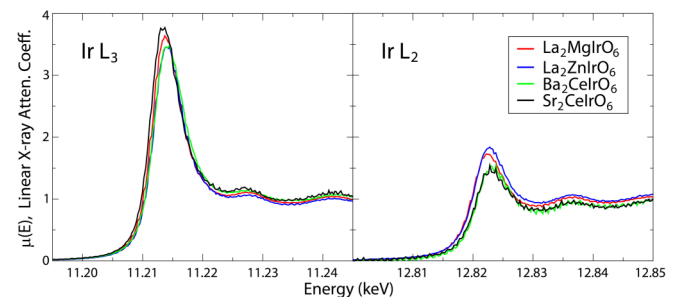

FIG. 3. X-ray absorption spectra collected at the Ir L_3 edge (left) and the Ir L_2 edge (right) for the double perovskite iridates La_2MgIrO_6, La_2ZnIrO_6, Ba_2CeIrO_6, and Sr_2CeIrO_6. Note the dramatic intensity difference between the sharp "white-line" features observed at the L_3 and L_2 absorption edges.

TABLE II. Branching ratios (BR) and expectation value of the spin-orbit coupling operator $\langle \boldsymbol{L} \cdot \boldsymbol{S} \rangle$ in units of $\hbar^2$ for selected d^5 iridates.

Material	BR	$\langle \boldsymbol{L} \cdot \boldsymbol{S} \rangle$	Ref.
La_2MgIrO_6	6.5(9)	3.0(6)	this work
La_2ZnIrO_6	4.5(5)	2.3(4)	this work
Ba_2CeIrO_6	6.8(9)	3.1(6)	this work
Sr_2CeIrO_6	6.3(7)	3.0(5)	this work
Sr_2TiIrO_6	4.04	2.02	[48]
La_2NiIrO_6	4.31	2.18	[48]
Sr_2IrO_4	7.0(4)	3.0(3)	[58]
$Sr_3Ir_2O_7$	5.5	2.69	[59]
Na_2IrO_3	5.7(3)	2.8(2)	[58]
α-Li_2IrO_3	5.1(4)	2.5(2)	[60]
$Y_2Ir_2O_7$	6.0(3)	2.9(2)	[58]

white-line intensity was also obtained from simple numerical integration, after modeling the absorption step by a unit step function fixed at the inflection point of $\mu(E)$. This numerical integration provides a useful consistency check for the fit results, as well as a measure of white-line intensity that is less sensitive to any line-shape asymmetry. The final values for the white-line intensities, and their corresponding BRs, reflect the average obtained from these two methods. The BRs and $\langle \boldsymbol{L} \cdot \boldsymbol{S} \rangle$ values extracted from this analysis are shown in Table II, where they are also compared to the values obtained from other selected d^5 iridates. The enhanced BRs for La_2MgIrO_6, La_2ZnIrO_6, Ba_2CeIrO_6, and Sr_2CeIrO_6 are within the range typically found for an Ir^{4+} ion in an octahedral local environment. These results indicate sizable orbital contributions to the Ir^{4+} electronic ground states in these materials, which is an essential ingredient for the realization of $J_{eff} = 1/2$ moments.

Unfortunately, establishing $J_{eff} = 1/2$ magnetism in d^5 iridates on the basis of BR measurements alone has proven to be extremely difficult. When the SOC coupling constant $\lambda \ll$ the cubic crystal-field splitting $10Dq$, one expects $\langle \boldsymbol{L} \cdot \boldsymbol{S} \rangle = \hbar^2$ for a $J_{eff} = 1/2$ state [61]. The $\langle \boldsymbol{L} \cdot \boldsymbol{S} \rangle$ values in Table II are significantly larger, even for established $J_{eff} = 1/2$ magnets like Sr_2IrO_4 and $Sr_3Ir_2O_7$. It is now well known that $\lambda \sim \frac{1}{6}10Dq$ is typical for d^5 iridates [59], and so the assumption made above to calculate the BR for a $J_{eff} = 1/2$ state may not be valid. Instead, significant mixing between the excited $J_{eff} = 3/2$ and e_g manifolds will yield enhanced BRs [61,62] with a range of possible material-dependent values even for $J_{eff} = 1/2$ magnets. This being said, the presence of a significantly enhanced BR does appear to be a good indicator of the $J_{eff} = 1/2$ state in several other candidate Kitaev materials. In particular, the pressure-induced collapse of the $J_{eff} = 1/2$ ground state in α-Li_2IrO_3 is accompanied by a rapid drop in the BR [60], which approaches that of elemental Ir (BR ~ 3) in its dimerized, non-J_{eff}, high-pressure state.

Resonant inelastic x-ray scattering (RIXS) provides a direct measurement of the electronic ground state and therefore offers a uniquely powerful way to assess the $J_{eff} = 1/2$ candidacy of the d^5 iridates. For an Ir^{4+} ion in an ideal octahedral environment, the $J_{eff} = 1/2$ doublet ground state is separated from the $J_{eff} = 3/2$ quartet excited state by $\frac{3}{2}\lambda$. Noncubic

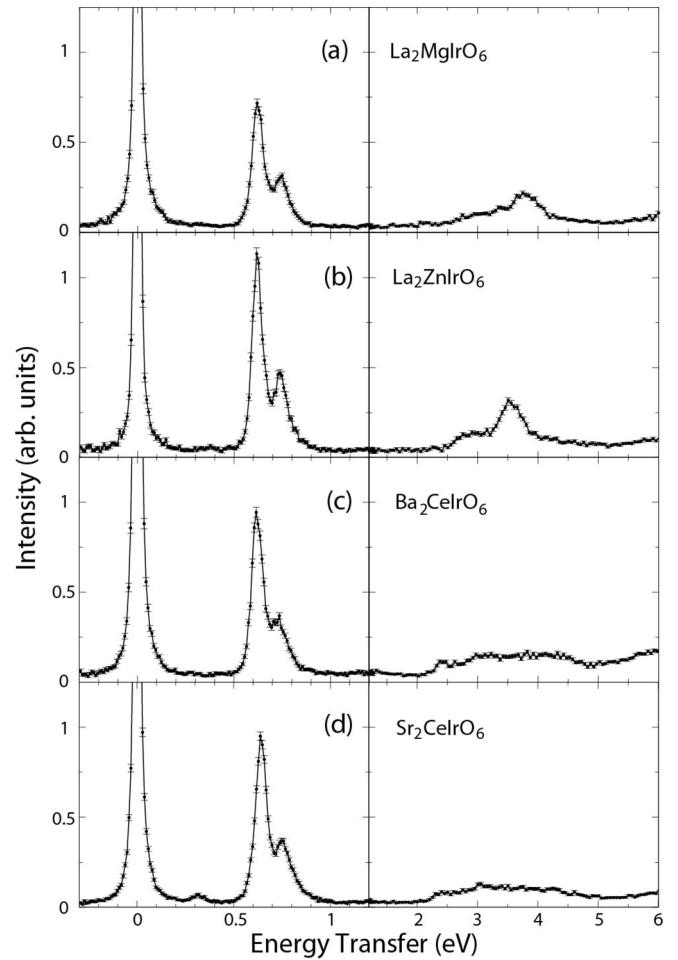FIG. 4. Resonant inelastic x-ray scattering spectra collected at the Ir L_3 edge ($E_i = 11.215$ keV) for (a) La_2MgIrO_6, (b) La_2ZnIrO_6, (c) Ba_2CeIrO_6, and (d) Sr_2CeIrO_6. Note the presence of a strong elastic line at an energy transfer $\hbar\omega = 0$, two peaks at energy transfers of $\hbar\omega \sim 0.6$–0.7 eV corresponding to intraband t_{2g} crystal-field transitions, and higher-energy excitations centered at $\hbar\omega \sim 3.5$ eV corresponding to interband t_{2g} to e_g crystal-field transitions.

crystal fields at the Ir^{4+} site will split the excited quartet into two doublets. RIXS can be used to probe these crystal-field excitations and therefore provides a direct measurement of λ and the noncubic crystal field Δ at the Ir^{4+} site.

Figure 4 presents the RIXS spectra at the Ir L_3 edge for La_2MgIrO_6, La_2ZnIrO_6, Ba_2CeIrO_6, and Sr_2CeIrO_6; two inelastic features are observed for each sample below 1 eV. The energy scale of these modes matches well with expectations for intraband t_{2g} crystal-field transitions in d^5 iridates [63]. We fit each spectrum to the sum of three Lorentzian functions representing the elastic line and the two intraband t_{2g} transitions. These fits were used to establish precise inelastic peak positions ($\hbar\omega_1$ and $\hbar\omega_2$) and therefore enable a meaningful quantitative comparison between the four samples; the fitting results are summarized in Table III. Several past studies on other iridates have extracted λ and Δ from $\hbar\omega_1$ and $\hbar\omega_2$ using a simple single-ion Hamiltonian with spin-orbit coupling and tetragonal crystal-field terms [64–66]. Since the DP iridates being considered here have a more complicated noncubic

TABLE III. RIXS fitting results of the intra-t_{2g} excitations, spin-orbit coupling constants (λ), and noncubic crystal-field splitting (Δ) of the $J_{\mathrm{eff}} = 3/2$ manifold for selected iridates and iridium fluorides. All parameters are in meV.

Material	$\hbar\omega_1$	$\hbar\omega_2$	λ	Δ	Ref.
La_2MgIrO_6	625(1)	744(2)	456(1)	119(2)	this work
La_2ZnIrO_6	624(1)	744(2)	456(1)	120(2)	this work
Ba_2CeIrO_6	625(1)	735(4)	453(1)	110(4)	this work
Sr_2CeIrO_6	645(1)	760(3)	468(1)	115(3)	this work
Sr_2IrO_4	550	700	417	150	[67]
$Sr_3Ir_2O_7$	500	700	400	200	[67]
Na_2IrO_3	720(20)	830(20)	517(9)	110(30)	[68]
α-Li_2IrO_3	720(20)	830(20)	517(9)	110(30)	[68]
$Y_2Ir_2O_7$	530(50)	980(50)	500(20)	450(70)	[65]
K_2IrF_6	802(1)	914(1)	572(1)	112(1)	[69]
Na_2IrF_6	816(1)	923(1)	580(1)	107(1)	[69]

crystal-field splitting, we adopt a different approach to estimate λ and Δ. We assume that the energy difference between $\hbar\omega_1$ and $\hbar\omega_2$ corresponds to Δ, while the average energy of these two peaks is $\frac{3}{2}\lambda$. We note that this method provides a reasonable estimation of λ, especially when $\Delta \leqslant 200$ meV [70].

Our results for λ and Δ are shown in Table III and compared to the values obtained for other selected iridates and iridium fluorides using this same approach. Sr_2CeIrO_6 has a slightly larger λ value as compared to the other three DP iridates, while Δ follows the general trend expected from NPD and increases as the Ir^{4+} local environment becomes progressively more distorted. The most surprising finding may be the presence of two intra-t_{2g} excitations in the Ba_2CeIrO_6 spectrum despite the assignment of $Fm\bar{3}m$ cubic symmetry from NPD, but this may arise due to a small global structural distortion that was not resolved by neutron diffraction or local distortions of the IrO_6 octahedra. Nonetheless, these results show that $\lambda/\Delta > 3.5$ for all four double perovskite iridates considered here, which places these materials in a similar regime to the well-established $J_{\mathrm{eff}} = 1/2$ magnet Sr_2IrO_4 ($\lambda/\Delta = 2.8$) [67] and the Kitaev materials Na_2IrO_3 and α-Li_2IrO_3 ($\lambda/\Delta = 4.7$) [68]. Taken together with the extremely small IrO_6 octahedral distortions determined by NPD and the enhanced branching ratio found by XAS, this is strong evidence that these double perovskite iridates host $J_{\mathrm{eff}} = 1/2$ electronic ground states.

It should be noted that there is a small inelastic feature present at $\hbar\omega \sim 0.32$ eV in the RIXS spectrum of Sr_2CeIrO_6. This peak does not appear in the low-energy excitation spectra of the other three DP compounds. Based on similar RIXS measurements carried out on the Ir^{5+} ($5d^4$) DP iridates Sr_2GdIrO_6 and Sr_2YIrO_6 [71], we attribute this 0.32 eV peak to the presence of a small amount of Ir^{5+} impurities. This energy scale is characteristic of the lowest-lying intra-t_{2g} excitations associated with Ir^{5+} ions, while the next branch of Ir^{5+} crystal-field excitations ($\hbar\omega \sim 0.66$ eV) would overlap with the much stronger intra-t_{2g} peaks from Ir^{4+}.

Interestingly, although the intraband t_{2g} crystal-field excitations in Fig. 4 are very similar in all four double perovskite compounds studied (in terms of peak position, peak splitting, and linewidth), there are quite obvious differences in the properties of the interband t_{2g} to e_g transitions. In particular, the t_{2g} to e_g excitations in Ba_2CeIrO_6 and Sr_2CeIrO_6 are much broader than those of La_2MgIrO_6 and La_2ZnIrO_6, indicating that the e_g energy levels must possess a much larger electronic bandwidth. This difference is quite surprising, given that the intra-t_{2g} excitations in the DP iridates appear to be largely insensitive to chemical composition or local structural details. At even higher energy transfers ($\hbar\omega \sim 6$ eV, not fully shown in Fig. 4), we observe a third set of transitions, which we attribute to charge-transfer excitations from the O $2p$ band to the Ir $5d$ band. The energy and width of these charge-transfer excitations appear to be almost identical in all compounds measured.

V. MAGNETIC STRUCTURES

Now that we have established $J_{\mathrm{eff}} = 1/2$ magnetism in La_2MgIrO_6, La_2ZnIrO_6, Ba_2CeIrO_6, and Sr_2CeIrO_6, it is fully anticipated that the classical phase diagram for the fcc Heisenberg-Kitaev-Γ model [37] should serve as a good starting point for explaining their magnetic properties. Although La_2MgIrO_6 and La_2ZnIrO_6 have already been investigated with this in mind [37,38], it is important to note that a unique magnetic structure solution for La_2MgIrO_6 has not been found. While previous NPD work has identified A-type magnetic order in La_2MgIrO_6 and La_2ZnIrO_6 [36], this is consistent with both the A-I and A-II states that appear in the phase diagram. Both spin arrangements consist of FM planes that are stacked in an AFM fashion and ordered moments that point along Ir-O bonds, but the moments are perpendicular to the FM planes in the A-I state and parallel to the FM planes in the A-II state. Unfortunately, NPD cannot be used to determine the magnetic moment direction due to the observation of only a single magnetic Bragg peak at $Q = 0.79$ Å^{-1} in each case. It is important to distinguish between the A-I and A-II states experimentally because they establish the sign of a possible Kitaev interaction in these materials [37]. More specifically, an AFM (FM) Kitaev interaction is only compatible with the A-II (A-I) state.

In the absence of single crystals, some progress can be made toward establishing a unique magnetic structure for La_2ZnIrO_6 by assuming that the ordered moment direction tracks the IrO_6 octahedral rotations, as previously proposed [11] and subsequently verified for Sr_2IrO_4 [72]. Although the single magnetic Bragg peak can be indexed in monoclinic notation with a magnetic propagation vector of either $\boldsymbol{k} = 0$ or (0.5 0.5 0), which correspond to A-type AFM ordered states with FM plane stacking directions parallel and perpendicular to the c axis, respectively, the observation of a net FM moment in the magnetization versus magnetic-field data [36] is only consistent with $\boldsymbol{k} = 0$. The single magnetic Bragg peak must then correspond to $\boldsymbol{Q} = (0\ 0\ 1)$, and its nonzero intensity is only compatible with an A-II structure due to neutron polarization factor arguments. On the other hand, similar reasoning cannot be used to differentiate between the A-I and A-II states for La_2MgIrO_6. The magnetization of this system increases linearly with magnetic field [36]. Since the IrO_6 octahedral rotations in these two materials are very similar, as
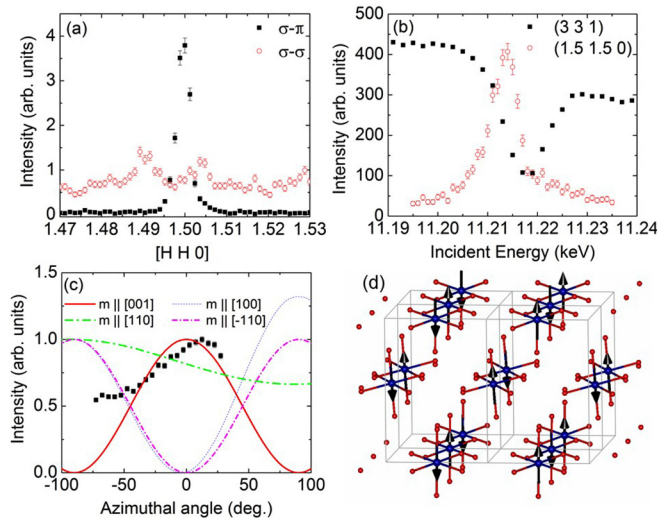
FIG. 5. Resonant magnetic x-ray scattering results on single crystalline La_2MgIrO_6. (a) The structurally forbidden Bragg peak (1.5 1.5 0) only appears in the σ-π scattering channel. (b) The same (1.5 1.5 0) peak shows a resonant enhancement just below the Ir L_3 absorption edge, while the (3 3 1) structural peak exhibits typical intensity modulation near the absorption edge. (c) The azimuthal intensity dependence of the (0.5 0.5 0) Bragg peak is best described by A-II AFM order with the Ir moments aligned very close to the crystalline c direction. (d) A schematic of the proposed magnetic structure for La_2MgIrO_6. It is anticipated that the Ir moments cant away from the c axis to track the small IrO_6 octahedral rotations.

shown in Table I, this implies that the magnetic propagation vector is $\boldsymbol{k} = (0.5\ 0.5\ 0)$. However, both $\boldsymbol{Q} = (0.5\ 0.5\ 0)$ or $(0.5\ -0.5\ 0)$ can contribute to the intensity of the single magnetic Bragg peak, which prevents straightforward differentiation between the A-I and A-II states. Single-crystal measurements are therefore required in this case.

Since we could not grow single crystals of La_2MgIrO_6 large enough for neutron diffraction, we performed a resonant magnetic x-ray scattering (RMXS) experiment to try and resolve this issue instead. With the photon energy tuned close to the L_3 edge and the sample cooled below T_N to 6 K, new Bragg peaks emerged that are consistent with the expected magnetic propagation vector $\boldsymbol{k} = (0.5\ 0.5\ 0)$. These extra peaks appear in the σ-π channel only, as shown in Fig. 5(a) for the representative (1.5 1.5 0) position. We also plot the energy dependence of this same peak and the structurally allowed (3 3 1) reflection in Fig. 5(b). There is clear resonant behavior at the (1.5 1.5 0) position near the energy corresponding to the L_3 edge, while typical intensity modulation near the absorption edge is found at the (3 3 1) position. Finally, we find that the resonant enhancement of the (1.5 1.5 0) peak occurs slightly below the XAS maximum as noted for the magnetic peaks previously identified by RMXS in Sr_2IrO_4 [73], Na_2IrO_3 [74], and $Sr_3Ir_2O_7$ [75]. These combined findings provide strong evidence that the (1.5 1.5 0) Bragg peak observed here has a magnetic origin.

We proceeded to measure the azimuthal intensity dependence of the (0.5 0.5 0) magnetic Bragg peak in an effort to differentiate between the A-I and A-II states described above. This approach involves rotating the sample around

the scattering vector $\boldsymbol{Q}$ in fixed increments and performing θ (i.e., rocking) scans at each of these different Ψ angles. It has been used successfully to determine the ordered moment direction with RMXS in other antiferromagnetic materials [76]. Figure 5(c) shows the integrated intensity of the (0.5 0.5 0) reflection as a function of Ψ with solid black squares; $\Psi = 0$ corresponds to the crystalline c axis. The azimuthal intensity modulation expected for four different moment directions, as calculated by the software package FDMNES [77], is also shown in this figure. The experimental data most closely resemble the calculation for ordered moments along the c direction, which allows us to conclude that La_2MgIrO_6 has an A-II ground state. A schematic of the magnetic structure for La_2MgIrO_6 is shown in Fig. 5(d).

Less information is known about the magnetic structures of Ba_2CeIrO_6 and Sr_2CeIrO_6. Previous bulk characterization studies have established AFM order in both materials with $T_N = 17$ and 21 K for the Ba [40] and Sr [41,43,46] analogs, respectively, but the specific spin configurations have not been determined. We first present magnetic susceptibility versus temperature measurements in Figs. 6(a) and 6(b) for both materials, which show that the magnetic ordering temperatures of our samples are in good agreement with previous work. We also present low-temperature magnetization versus field data in Figs. 6(c) and 6(d), which show the same linear behavior observed previously for La_2MgIrO_6 but not La_2ZnIrO_6.

Since no magnetic Bragg peaks were observed in the HB-2A data, we collected complementary elastic neutron scattering data on the HB-1A triple-axis spectrometer. This instrument has an excellent signal-to-noise ratio and therefore is extremely useful for investigating materials with weak magnetic signals [78]. Representative data indicated by the solid symbols and obtained at both 4 and 30 K are shown in Fig. 6(e) for Sr_2CeIrO_6 and Fig. 6(f) for Ba_2CeIrO_6. Two new peaks are visible in the 4 K dataset of each material, and the order-parameter plots presented in Figs. 6(g) and 6(h) indicate that they have a magnetic origin. To refine the magnetic structures with FULLPROF, we first fixed all of the structural parameters to the values obtained from the HB-2A refinements and then obtained an overall scale factor using the nuclear Bragg peaks measured with HB-1A (not shown here).

Although the magnetic Bragg peaks of Sr_2CeIrO_6 can be indexed with either the A-type AFM propagation vector $\boldsymbol{k} = 0$ or (0.5 0.5 0), the lack of a net FM moment despite the significant IrO_6 octahedral rotations is only consistent with the latter. The two magnetic Bragg peaks of Ba_2CeIrO_6 can also be attributed to A-type AFM, which has a propagation vector of $\boldsymbol{k} = (0\ 0\ 1)$ for an ideal fcc structure. Therefore, we tried refinements with the appropriate propagation vector for each material using both A-I and A-II spin configurations. The Ir^{4+} magnetic form factor, $j_0(Q)$, was taken from Ref. [79]. The results are superimposed on the data shown in Figs. 6(e) and 6(f) for the Sr and Ba systems, respectively, and indicate that the relative intensities of the two magnetic peaks are captured much better by the A-II model in each case. Our best refinements yield ordered moments of $0.5(1)\mu_B$ for Sr_2CeIrO_6 and $0.3(1)\mu_B$ for Ba_2CeIrO_6. With A-II magnetic structures now established for both La_2MgIrO_6 and La_2ZnIrO_6, we also refined the ordered moment size for these materials using data from the neutron scattering

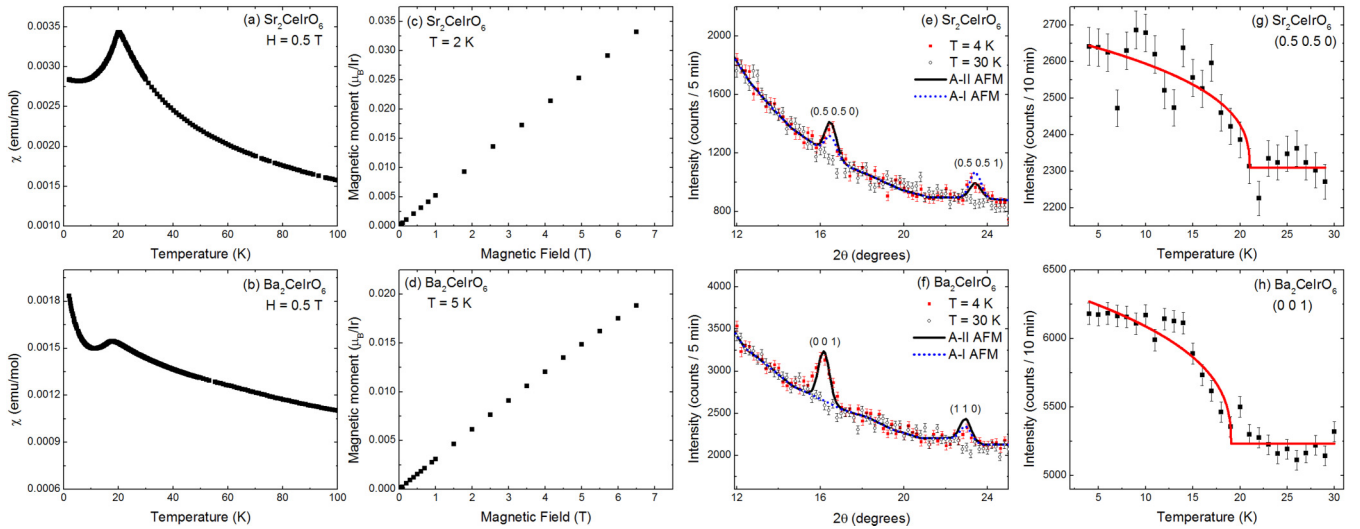FIG. 6. Bulk characterization and neutron powder diffraction (NPD) measurements on polycrystalline Sr_2CeIrO_6 and Ba_2CeIrO_6. (a),(b) Magnetic susceptibility measurements as a function of temperature reveal ordering temperatures $T_N = 21$ and 17 K for the Sr and Ba analogs, respectively, which is in good agreement with previous work [40,41]. (c),(d) The magnetization of both materials increases linearly with field. (e),(f) Neutron powder diffraction data are presented for both materials at $T = 4$ and 30 K. Two different refinement results are superimposed (solid and dotted curves) on the Sr_2CeIrO_6 and Ba_2CeIrO_6 data that are consistent with the field dependence of the magnetization. The A-II AFM model provides superior agreement with the NPD data in both cases. (g),(h) Order-parameter plots for the most intense magnetic Bragg peak observed in each case. The T_N values are consistent with the magnetic susceptibility results. Power-law curves are superimposed on the data as a guide to the eye.

experiments described in Ref. [36]. We found an ordered moment of $0.6(1)\mu_B$ for La_2MgIrO_6 and an ordered moment of $0.3(1)\mu_B$ for La_2ZnIrO_6. The common A-II AFM order in these four materials is likely driven by a significant AFM Kitaev interaction.

VI. MAGNETIC HAMILTONIANS

Perhaps the most interesting aspect of La_2MgIrO_6 and La_2ZnIrO_6 is that their thermodynamic properties, A-II ordered states, and gapped magnetic excitation spectra can be explained by a Heisenberg-Kitaev Hamiltonian with a dominant AFM Kitaev term [37,38]. Unfortunately, the monoclinic structural distortions of these materials ensure that competing Heisenberg-Ising models cannot be ruled out based on symmetry grounds alone, and different spin gap origins become viable within the Heisenberg-Kitaev models [38]. Since a common microscopic mechanism appears to be driving the magnetism of Ba_2CeIrO_6, Sr_2CeIrO_6, La_2MgIrO_6, and La_2ZnIrO_6, as indicated by the realization of $J_{eff} = 1/2$ moments and A-II AFM order in all four materials, a systematic study of their spin waves may allow one to place more stringent constraints on possible model Hamiltonians and spin-gap mechanisms.

Previously, we had great success measuring the magnetic excitation spectra of polycrystalline La_2MgIrO_6 and La_2ZnIrO_6 by performing an inelastic neutron scattering experiment at the HYSPEC spectrometer [38]. Therefore, we used the same experimental setup to investigate the spin dynamics of Ba_2CeIrO_6 and Sr_2CeIrO_6. Our main results are summarized in Fig. 7; color contour plots for Ba_2CeIrO_6 and Sr_2CeIrO_6 are presented with an incident energy $E_i = 15$ meV and temperatures both above and

below T_N. Inelastic spectra were also collected for both materials at the same temperatures with $E_i = 7.5$ meV (not shown). Surprisingly, in sharp contrast to our previous work on La_2MgIrO_6 and La_2ZnIrO_6, no clear magnetic signal is observed in these data, thus precluding detailed comparisons of the spin dynamics of these four materials.

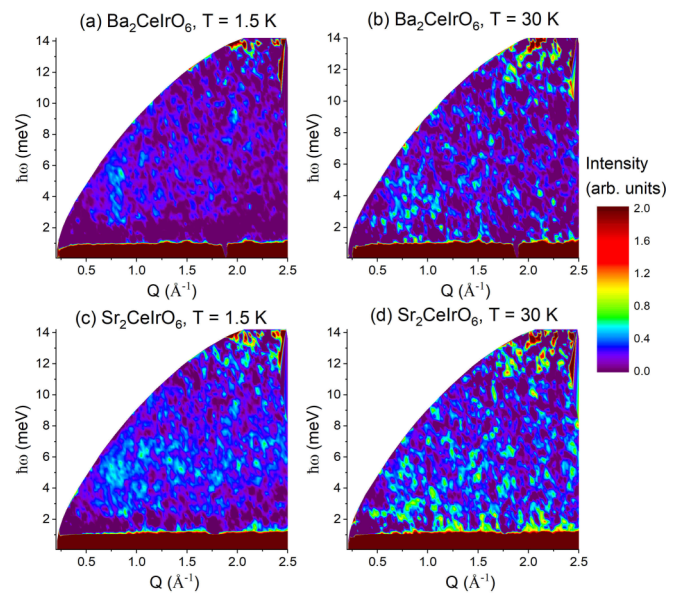FIG. 7. Color contour plots of the $E_i = 15$ meV HYSPEC data for Ba_2CeIrO_6 at (a) $T = 1.5$ K and (b) $T = 30$ K. Similar plots are shown in (c) and (d) for Sr_2CeIrO_6. In sharp contrast to previous work on La_2MgIrO_6 and La_2ZnIrO_6 [38], no clear magnetic excitations are visible in these spectra.

This difference in the inelastic spectra of the Ce and La samples is observed despite their similar ordered moments. The higher magnetic ordering temperatures of Ba_2CeIrO_6 and Sr_2CeIrO_6, as compared to La_2MgIrO_6 and La_2ZnIrO_6, imply larger exchange interactions in the Ce samples and hence an increased spin-wave bandwidth. As these excitations become more dispersive, they will be harder to detect for a comparable signal-to-noise ratio, and this may be the reason that they were not observed in the Ba_2CeIrO_6 and Sr_2CeIrO_6 spectra. Single-crystal measurements are therefore required to measure the spin waves in the Ce samples with INS.

VII. CONCLUSIONS

By providing strong experimental evidence for Ir^{4+} $J_{eff} = 1/2$ electronic ground states in the double perovskite iridates La_2MgIrO_6, La_2ZnIrO_6, Ba_2CeIrO_6, and Sr_2CeIrO_6, we showed that the classical phase diagram for the fcc Heisenberg-Kitaev-Γ model discussed in Ref. [37] should provide an excellent starting point for explaining their collective magnetic properties. We strengthened this conjecture by identifying magnetic structures in these materials that appear on this phase diagram. More specifically, our scattering results on La_2MgIrO_6, Sr_2CeIrO_6, and Ba_2CeIrO_6 establish A-II AFM order in these materials, which was previously identified for La_2ZnIrO_6 [38]. We anticipate that this magnetic ground state arises from a significant AFM Kitaev interaction that is common to all four of these double perovskite iridates.

Attempts to determine the magnetic Hamiltonian for Ba_2CeIrO_6 and Sr_2CeIrO_6 with inelastic neutron scattering and therefore prove this hypothesis were unsuccessful, as no magnetic excitations were observed in these data. Nonetheless, our combined results reported here elucidate the extreme similarities in the electronic and magnetic properties of these four systems, and they suggest that spacing $J_{eff} = 1/2$ magnetic atoms further apart is a promising way to find new Kitaev material candidates with lattice geometries beyond honeycomb. The fcc magnets A_2IrX_6, where $A = $ Na, K, Rb, or Cs and $X = $ F [69] or Cl [80,81], are particularly attractive in this regard, as adjacent IrX_6 octahedra are arranged in the appropriate geometry required to realize significant Kitaev interactions through extended superexchange pathways, and ideal cubic systems may exist [80,81].

Note added. Recently, we noticed that a related study on Ba_2CeIrO_6 is available in Ref. [82]. In that work, the authors report single-crystal x-ray diffraction data that are well described by the $Fm\bar{3}m$ space group and RIXS measurements of the intraband t_{2g} crystal field excitations that support a $J_{eff} = 1/2$ electronic ground state. They also perform theoretical calculations to show that the magnetic Hamiltonian for Ba_2CeIrO_6 consists of a significant AFM Kitaev interaction. These results are all consistent with the conclusions reported in our paper. The main difference between the two works is that we find an experimental magnetic propagation vector $\boldsymbol{k} = (0\ 0\ 1)$, while the theoretical calculations in Ref. [82] predict $\boldsymbol{k} = (0\ 0.5\ 1)$.

[1] S. Trebst, arXiv:1701.07056.

[2] S. M. Winter, A. A. Tsirlin, M. Daghofer, J. van den Brink, Y. Singh, P. Gegenwart, and R. Valenti, J. Phys.: Condens. Matter **29**, 493002 (2017).

[3] A. Kitaev, Ann. Phys. **321**, 2 (2006).

[4] E. K.-H. Lee, R. Schaffer, S. Bhattacharjee, and Y. B. Kim, Phys. Rev. B **89**, 045117 (2014).

[5] I. Kimchi, J. G. Analytis, and A. Vishwanath, Phys. Rev. B **90**, 205126 (2014).

[6] K. Li, S.-L. Yu, and J.-X. Li, New J. Phys. **17**, 043032 (2015).

[7] A. Catuneanu, J. G. Rau, H.-S. Kim, and H.-Y. Kee, Phys. Rev. B **92**, 165108 (2015).

[8] M. Becker, M. Hermanns, B. Bauer, M. Garst, and S. Trebst, Phys. Rev. B **91**, 155135 (2015).

[9] K. Shinjo, S. Sota, S. Yunoki, K. Totsuka, and T. Tohyama, J. Phys. Soc. Jpn. **85**, 114710 (2016).

[10] I. Kimchi and A. Vishwanath, Phys. Rev. B **89**, 014414 (2014).

[11] G. Jackeli and G. Khaliullin, Phys. Rev. Lett. **102**, 017205 (2009).

[12] B. J. Kim, H. Jin, S. J. Moon, J.-Y. Kim, B.-G. Park, C. S. Leem, J. Yu, T. W. Noh, C. Kim, S.-J. Oh, J.-H. Park, V. Durairaj, G. Cao, and E. Rotenberg, Phys. Rev. Lett. **101**, 076402 (2008).

[13] Y. Singh and P. Gegenwart, Phys. Rev. B **82**, 064412 (2010).

[14] H.-C. Jiang, Z.-C. Gu, X.-L. Qi, and S. Trebst, Phys. Rev. B **83**, 245104 (2011).

[15] Y. Singh, S. Manni, J. Reuther, T. Berlijn, R. Thomale, W. Ku, S. Trebst, and P. Gegenwart, Phys. Rev. Lett. **108**, 127203 (2012).

[16] G. Cao, T. F. Qi, L. Li, J. Terzic, V. S. Cao, S. J. Yuan, M. Tovar, G. Murthy, and R. K. Kaul, Phys. Rev. B **88**, 220414(R) (2013).

[17] K. W. Plumb, J. P. Clancy, L. J. Sandilands, V. V. Shankar, Y. F. Hu, K. S. Burch, H.-Y. Kee, and Y.-J. Kim, Phys. Rev. B **90**, 041112(R) (2014).

[18] R. D. Johnson, S. C. Williams, A. A. Haghighirad, J. Singleton, V. Zapf, P. Manuel, I. I. Mazin, Y. Li, H. O. Jeschke, R. Valenti, and R. Coldea, Phys. Rev. B **92**, 235119 (2015).

[19] J. A. Sears, M. Songvilay, K. W. Plumb, J. P. Clancy, Y. Qiu, Y. Zhao, D. Parshall, and Y.-J. Kim, Phys. Rev. B **91**, 144420 (2015).

[20] A. Banerjee, C. A. Bridges, J.-Q. Yan, A. A. Aczel, L. Li, M. B. Stone, G. E. Granroth, M. D. Lumsden, Y. Yiu, J. Knolle, S. Bhattacharjee, D. L. Kovrizhin, R. Moessner, D. A. Tennant, D. G. Mandrus, and S. E. Nagler, Nat. Mater. **15**, 733 (2016).

[21] T. Takayama, A. Kato, R. Dinnebier, J. Nuss, H. Kono, L. S. I. Veiga, G. Fabbris, D. Haskel, and H. Takagi, Phys. Rev. Lett. **114**, 077202 (2015).

[22] A. Biffin, R. D. Johnson, S. Choi, F. Freund, S. Manni, A. Bombardi, P. Manuel, P. Gegenwart, and R. Coldea, Phys. Rev. B **90**, 205116 (2014).

[23] K. A. Modic, T. E. Smidt, I. Kimchi, N. P. Breznay, A. Biffin, S. Choi, R. D. Johnson, R. Coldea, P. Watkins-Curry, G. T. McCandless, J. Y. Chan, F. Gandara, Z. Islam, A. Vishwanath, A. Shekhter, R. D. McDonald, and J. G. Analytis, Nat. Commun. **5**, 4203 (2014).

[24] A. Biffin, R. D. Johnson, I. Kimchi, R. Morris, A. Bombardi, J. G. Analytis, A. Vishwanath, and R. Coldea, Phys. Rev. Lett. **113**, 197201 (2014).

[25] A. Banerjee, J.-Q. Yan, J. Knolle, C. A. Bridges, M. B. Stone, M. D. Lumsden, D. G. Mandrus, D. A. Tennant, R. Moessner, and S. E. Nagler, Science **356**, 1055 (2017).

[26] L. J. Sandilands, Y. Tian, K. W. Plumb, Y.-J. Kim, and K. S. Burch, Phys. Rev. Lett. **114**, 147201 (2015).

[27] A. Banerjee, P. Lampen-Kelley, J. Knolle, C. Balz, A. A. Aczel, B. Winn, Y. Liu, D. Pajerowski, J.-Q. Yan, C. A. Bridges, A. T. Savici, B. C. Chakoumakos, M. D. Lumsden, D. A. Tennant, R. Moessner, D. G. Mandrus, and S. E. Nagler, npj Quantum Mater. **3**, 8 (2018).

[28] P. Lampen-Kelley, A. Banerjee, A. A. Aczel, H. B. Cao, M. B. Stone, C. A. Bridges, J.-Q. Yan, S. E. Nagler, and D. Mandrus, Phys. Rev. Lett. **119**, 237203 (2017).

[29] Y. Cui, J. Zheng, K. Ran, J. Wen, Z.-X. Liu, B. Liu, W. Guo, and W. Yu, Phys. Rev. B **96**, 205147 (2017).

[30] M. Abramchuk, C. Ozsoy-Keskinbora, J. W. Krizan, K. R. Metz, D. C. Bell, and F. Tafti, J. Am. Chem. Soc. **139**, 15371 (2017).

[31] K. Kitagawa, T. Takayama, Y. Matsumoto, A. Kato, R. Takano, Y. Kishimoto, S. Bette, R. Dinnebier, G. Jackeli, and H. Takagi, Nature (London) **554**, 341 (2018).

[32] E. M. Kenney, C. U. Segre, W. Lafargue-Dit-Hauret, O. I. Lebedev, M. Abramchuk, A. Berlie, S. P. Cottrell, G. Simutis, F. Bahrami, N. E. Mordvinova, J. L. McChesney, G. Fabbris, D. Haskel, X. Rocquefelte, M. J. Graf, and F. Tafti, arXiv:1811.00565.

[33] Y. S. Choi, C. H. Lee, S. Lee, S. Yoon, W.-J. Lee, J. Park, A. Ali, Y. Singh, J.-C. Orain, G. Kim, J.-S. Rhyee, W.-T. Chen, F. Chou, and K.-Y. Choi, arXiv:1811.07002.

[34] T. Dey, A. V. Mahajan, P. Khuntia, M. Baenitz, B. Koteswararao, and F. C. Chou, Phys. Rev. B **86**, 140405(R) (2012).

[35] W.-J. Lee, S.-H. Do, S. Yoon, S. Lee, Y. S. Choi, D. J. Jang, M. Brando, M. Lee, E. S. Choi, S. Ji, Z. H. Jang, B. J. Suh, and K.-Y. Choi, Phys. Rev. B **96**, 014432 (2017).

[36] G. Cao, A. Subedi, S. Calder, J.-Q. Yan, J. Yi, Z. Gai, L. Poudel, D. J. Singh, M. D. Lumsden, A. D. Christianson, B. C. Sales, and D. Mandrus, Phys. Rev. B **87**, 155136 (2013).

[37] A. M. Cook, S. Matern, C. Hickey, A. A. Aczel, and A. Paramekanti, Phys. Rev. B **92**, 020417(R) (2015).

[38] A. A. Aczel, A. M. Cook, T. J. Williams, S. Calder, A. D. Christianson, G.-X. Cao, D. Mandrus, Y.-B. Kim, and A. Paramekanti, Phys. Rev. B **93**, 214426 (2016).

[39] P. D. Battle and J. G. Gore, J. Mater. Chem. **6**, 1375 (1996).

[40] M. Wakeshima, D. Harada, and Y. Hinatsu, J. Mater. Chem. **10**, 419 (2000).

[41] D. Harada, M. Wakeshima, and Y. Hinatsu, J. Solid State Chem. **145**, 356 (1999).

[42] S. K. Panda and I. Dasgupta, Mod. Phys. Lett. B **27**, 1350041 (2013).

[43] S. Kanungo, K. Mogare, B. Yan, M. Reehuis, A. Hoser, C. Felser, and M. Jansen, Phys. Rev. B **93**, 245148 (2016).

[44] E. M. Ramos, I. Alvarez, M. L. Viega, and C. Pico, J. Mater. Sci. Lett. **14**, 1577 (1995).

[45] R. C. Currie, J. F. Vente, E. Frikkee, and D. J. W. Ijdo, J. Solid State Chem. **116**, 199 (1995).

[46] D. Harada, M. Wakeshima, Y. Hinatsu, K. Ohoyama, and Y. Yamaguchi, J. Phys.: Condens. Matter **12**, 3229 (2000).

[47] J. Rodriguez-Carvajal, Physica B **192**, 55 (1993).

[48] M. A. Laguna-Marco, P. Kayser, J. A. Alonso, M. J. Martinez-Lope, M. van Veenendaal, Y. Choi, and D. Haskel, Phys. Rev. B **91**, 214433 (2015).

[49] R. D. Shannon, Acta Crystallogr. **A32**, 751 (1976).

[50] F. Ye, S. Chi, H. Cao, B. C. Chakoumakos, J. A. Fernandez-Baca, R. Custelcean, T. F. Qi, O. B. Korneta, and G. Cao, Phys. Rev. B **85**, 180403(R) (2012).

[51] M. K. Crawford, M. A. Subramanian, R. L. Harlow, J. A. Fernandez-Baca, Z. R. Wang, and D. C. Johnston, Phys. Rev. B **49**, 9198 (1994).

[52] W. A. Groen, F. P. F. van Berkel, and D. J. W. Ijdo, Acta Crystallogr. C **42**, 1472 (1986).

[53] A. M. Glazer, Acta Crystallogr. B **28**, 3384 (1972).

[54] P. M. Woodward, Acta. Crystallogr. B **53**, 32 (1997).

[55] G. van der Laan and B. T. Thole, Phys. Rev. Lett. **60**, 1977 (1988).

[56] B. T. Thole and G. van der Laan, Phys. Rev. B **38**, 3158 (1988).

[57] B. T. Thole and G. van der Laan, Phys. Rev. A **38**, 1943 (1988).

[58] J. P. Clancy, N. Chen, C. Y. Kim, W. F. Chen, K. W. Plumb, B. C. Jeon, T. W. Noh, and Y.-J. Kim, Phys. Rev. B **86**, 195131 (2012).

[59] C. Donnerer, M. Moretti Sala, S. Pascarelli, A. D. Rosa, S. N. Andreev, V. V. Mazurenko, T. Irifune, E. C. Hunter, R. S. Perry, and D. F. McMorrow, Phys. Rev. B **97**, 035106 (2018).

[60] J. P. Clancy, H. Gretarsson, J. A. Sears, Y. Singh, S. Desgreniers, K. Mehlawat, S. Layek, G. K. Rozenberg, Y. Ding, M. H. Upton, D. Casa, N. Chen, J. Im, Y. Lee, R. Yadav, L. Hozoi, D. Efremov, J. van den Brink, and Y.-J. Kim, npj Quantum Mater. **3**, 35 (2018).

[61] M. A. Laguna-Marco, D. Haskel, N. Souza-Neto, J. C. Lang, V. V. Krishnamurthy, S. Chikara, G. Cao, and M. van Veenendaal, Phys. Rev. Lett. **105**, 216407 (2010).

[62] G. L. Stamokostas and G. A. Fiete, Phys. Rev. B **97**, 085150 (2018).

[63] Y.-J. Kim, J. P. Clancy, H. Gretarsson, G. Cao, Y. Singh, J. Kim, M. H. Upton, D. Casa, and T. Gog, arXiv:1805.03612.

[64] X. Liu, V. M. Katukuri, L. Hozoi, W.-G. Yin, M. P. M. Dean, M. H. Upton, J. Kim, D. Casa, A. Said, T. Gog, T. F. Qi, G. Cao, A. M. Tsvelik, J. van den Brink, and J. P. Hill, Phys. Rev. Lett. **109**, 157401 (2012).

[65] L. Hozoi, H. Gretarsson, J. P. Clancy, B.-G. Jeon, B. Lee, K. H. Kim, V. Yushankhai, P. Fulde, D. Casa, T. Gog, J. Kim, A. H. Said, M. H. Upton, Y.-J. Kim, and J. van den Brink, Phys. Rev. B **89**, 115111 (2014).

[66] M. Moretti Sala, K. Ohgushi, A. Al-Zein, Y. Hirata, G. Monaco, and M. Krisch, Phys. Rev. Lett. **112**, 176402 (2014).

[67] X. Lu, P. Olalde-Velasco, Y. Huang, V. Bisogni, J. Pelliciari, S. Fatale, M. Dantz, J. G. Vale, E. C. Hunter, J. Chang, V. N. Strocov, R. S. Perry, M. Grioni, D. F. McMorrow, H. M. Ronnow, and T. Schmitt, Phys. Rev. B **97**, 041102(R) (2018).

[68] H. Gretarsson, J. P. Clancy, X. Liu, J. P. Hill, E. Bozin, Y. Singh, S. Manni, P. Gegenwart, J. Kim, A. H. Said, D. Casa, T. Gog, M. H. Upton, H.-S. Kim, J. Yu, V. M. Katukuri, L. Hozoi, J. van den Brink, and Y.-J. Kim, Phys. Rev. Lett. **110**, 076402 (2013).

[69] M. Rossi, M. Retegan, C. Giacobbe, R. Fumagalli, A. Efimenko, T. Kulka, K. Wohlfeld, A. I. Gubanov, and M. Moretti Sala, Phys. Rev. B **95**, 235161 (2017).

[70] M. Moretti Sala, S. Boseggia, D. F. McMorrow, and G. Monaco, Phys. Rev. Lett. **112**, 026403 (2014).

[71] B. Yuan, J. P. Clancy, A. M. Cook, C. M. Thompson, J. Greedan, G. Cao, B. C. Jeon, T. W. Noh, M. H. Upton, D. Casa, T. Gog, A. Paramekanti, and Y.-J. Kim, Phys. Rev. B **95**, 235114 (2017).

[72] S. Boseggia, H. C. Walker, J. Vale, R. Springell, Z. Feng, R. S. Perry, M. Moretti Sala, H. M. Ronnow, S. P. Collins, and D. F. McMorrow, J. Phys.: Condens. Matter **25**, 422202 (2013).

[73] B. J. Kim, H. Ohsumi, T. Komesu, S. Sakai, T. Morita, H. Takagi, and T. Arima, Science **323**, 1329 (2009).

[74] X. Liu, T. Berlijn, W.-G. Yin, W. Ku, A. Tsvelik, Y.-J. Kim, H. Gretarsson, Y. Singh, P. Gegenwart, and J. P. Hill, Phys. Rev. B **83**, 220403(R) (2011).

[75] S. Boseggia, R. Springell, H. C. Walker, A. T. Boothroyd, D. Prabhakaran, D. Wermeille, L. Bouchenoire, S. P. Collins, and D. F. McMorrow, Phys. Rev. B **85**, 184432 (2012).

[76] S. Boseggia, R. Springell, H. C. Walker, H. M. Ronnow, Ch. Ruegg, H. Okabe, M. Isobe, R. S. Perry, S. P. Collins, and D. F. McMorrow, Phys. Rev. Lett. **110**, 117207 (2013).

[77] Y. Joly, Phys. Rev. B **63**, 125120 (2001).

[78] J. Xiong, J.-Q. Yan, A. A. Aczel, and P. M. Woodward, J. Solid Chem. **258**, 762 (2018).

[79] K. Kobayashi, T. Nagao, and M. Ito, Acta Crystallogr. **A67**, 473 (2011).

[80] M. T. Hutchings and C. G. Windsor, Proc. Phys. Soc. **91**, 928 (1967).

[81] J. W. Lynn, G. Shirane, and M. Blume, Phys. Rev. Lett. **37**, 154 (1976).

[82] A. Revelli, C. C. Loo, D. Kiese, P. Becker, T. Frohlich, T. Lorenz, M. Moretti Sala, G. Monaco, F. L. Buessen, J. Attig, M. Hermanns, S. V. Streltsov, D. I. Khomskii, J. van den Brink, M. Braden, P. H. M. van Loosdrecht, S. Trebst, A. Paramekanti, and M. Gruninger, arXiv:1901.06215.